JOURNAL OF MATERIALS SCIENCE 31 (1996) 5915–5932

Microstructural aspects of hypervelocity impact cratering and jetting in copper

L. E. MURR, E. P. GARCIA, E. FERREYRA T., C-S. NIOU, J. M. RIVAS, S. A. QUIÑONES
Department of Metallurgical and Materials Engineering, The University of Texas at El Paso, El Paso, TX 79968, USA

Light and transmission electron microscopy techniques have been applied in observations of hypervelocity impact craters in two different copper targets: a 38 μm grain size mill-processed target, and a 763 μm grain size annealed target, the smaller grained target being impacted with a 1100 aluminium sphere and the larger grained target being impacted with a soda–lime glass sphere, at velocities near 6 km s^{-1}. Both target craters exhibited dynamic recrystallization near the crater wall. The jetting associated with these two craters was very different. Considerably more plastic flow and a larger rim characterized the larger grained target. No significant melt-related phenomena were observed either near the crater wall or in the jetted rim for either crater. Consequently, the principal features of crater formation involve extreme plastic flow in the solid state. Microbands were observed to occur profusely in a zone below the smaller grained mill-processed target crater while more profuse and extremely long, unidirectional bundles of microbands (which were coincident with traces of {1 1 1} planes) occurred below the annealed larger grained target crater. These observations attest to the dominant and unique role played by deformation microbands in cratering in copper, because essentially no deformation twins were observed in either target.

1. Introduction

In some preliminary research reported recently, we have observed that the microstructures below the crater wall and along the impact axis for hypervelocity impact craters in copper targets are not only diverse, but occur in zones which vary with impact velocity [1–3]. More importantly, there is no indication of melting or a melt zone. Dynamic recrystallization occurs adjacent to the crater wall, and the extent of this zone increases from the crater wall with increasing impact velocity. In copper targets examined previously [1–3], no deformation twinning was observed. However, a zone of microbands, which also increased in width and extent along the impact axis as the impact velocity increased, was observed. Neither the reason for the microbands instead of deformation twins, nor their mechanism of formation in the context of hypervelocity impact cratering, was known.

Although cratering in metal targets has a wide range of important applications, including military armour penetration phenomena and micrometeoroid impact phenomena in space, it has received no real attention from a fundamental materials perspective until only recently [1–3]. Penetration, in a classical sense, has been generally considered to be of the form $l(\rho_p/\rho_t)^{1/2}$, where l is either the penetrator length or diameter, and ρ_p and ρ_t are the penetrator and target densities, respectively. Cratering in metals has been considered for decades only in the context of residual (or final) crater dimensions versus the velocities of impact, penetrator diameter (as an ideal sphere), and the corresponding densities noted previously. Early work by Charters and Summers [4] produced an empirical approximation for the ratio of crater depth, p, to penetrating particle diameter, d_p, in the form

$$p/d_p = 2.28\,(\rho_p/\rho_t)^{2/3}(u_o/C_t)^{2/3} \quad (1)$$

where u_o is the impact velocity and C_t is the bulk sound velocity in the target. This equation was developed for a number of metal targets. Charters and Summers [4] also proposed that, because crater growth seemed to be stopped as a consequence of the target yield strength, σ_t, this term should probably replace C_t in the previous equation. Indeed, in more recent work by Cour-Palais [5, 6] and others [7], cratering equations have evolved in the general form

$$p/d_p = \zeta^*(u_o/\sigma_t)^{1/3} \quad (2)$$

for ballistic velocities of impact, and $p/d_p \doteq \zeta^*(u_o/\sigma_t^{1/2})^{2/3}$ for hypervelocity impact ($u_o \gtrsim 5$ km s^{-1}) where ζ^* is a constant (possibly different in each case), and contains the density ratio and other adjustable coefficients.

Treatments of cratering phenomena, including micrometeoroid impact craters in metal structures in space, have often followed those developed somewhat historically for geological processes [8]. In these processes, cratering is generally divided into three regimes: contact by the impacting projectile and compression of the target, excavation, and modification. In

0022–2461 © *1996 Chapman & Hall*

general, cratering, especially in the hypervelocity regime ($u_o > 5\ km\ s^{-1}$), involves the creation of spherical shock waves at the point of contact of the projectile and the target. These shock waves propagate into both the projectile and the target and both begin simultaneously to distort in shape as the projectile penetrates into the target. The target shock wave pressure far exceeds its yield stress and it is heavily deformed as the propagating wave approximates a hemisphere centred roughly a particle diameter below the original target surface [7–10]. Target material streams radially outward and upward along the growing crater wall. The projectile begins to melt and vaporize along with a purported melt zone at the crater surface whose thickness depends upon the impact velocity and the impacting particle size, d_p. The crater becomes hemispherical in a relatively short time with the depth of penetration ceasing before radial growth ceases. Melosh [8] notes that the crater is lined with melt at all stages of its expansion and this melt is jetted out of the crater, forming a raised rim which can shed or eject material by particulation around its perimeter. This process of jetting is often contrasted with shaped charge and related jetting processes. Melosh [8] contends that melt in jets occurs at very low velocities because so-called stagnation point pressures often exceed the impact point pressures by a factor 2 or more. As a consequence, jetting in a shaped charge will impose conditions conducive to melt, i.e. a pressure multiplication-induced melt.

Recent work has demonstrated that in the case of shaped charge jetting, melting is not generally observed, and shaped charge jets form by plastic (solid-state) flow [11–16]. The examination of the microstructure of shaped charge jet fragments has shown compelling evidence for dynamic recrystallization, which may, in fact, contribute to, or constitute, the mechanism of plastic flow in jet elongation [13, 17]. Our preliminary examinations of the microstructure extending along a narrow region coincident with the impact axis for craters in copper targets, have also revealed a zone of dynamic recrystallization [1–3]. Consequently, this begs the question of whether, in fact, hypervelocity impact cratering in metal targets, especially copper, involves any significant melt phenomena, and whether crater formation, including jetting, is dominated by plastic flow rather than melt-dominated flow.

Finally, it might be noted that Ferreyra *et al.* [18] have recently observed cratering effects as a consequence of specific microstructures in copper targets. In this work, both the grain size and the dislocation density were changed independently by roughly an order of magnitude. The dislocation density appeared to dominate not only the target hardness (and consequently the static yield stress) but also the cratering process. As a consequence, the cratering ratios described previously have been confirmed not only in terms of yield stress but also the specific microstructural features which contribute to the yield stress. Moreover, these observations confirm the earlier conclusions of Charters and Summers [4] that the target yield strength influences, and in fact stops, crater growth.

It was the intent of this investigation to critically examine and compare two residual crater microstructures: one corresponding to a 1100 aluminium (3.2 mm diameter) projectile impacting a 38 μm grain-sized copper target at a velocity of $6.01\ km\ s^{-1}$; the other corresponding to a 3.2 mm soda–lime glass sphere impacting a 763 μm grain-sized copper target at a velocity of $5.83\ km\ s^{-1}$. This critical examination involves light microscope observations of the complete crater wall area, extending into the crater rims, in cross-sectional samples. Transmission electron microscope views of selected cross-sectional areas below the crater wall and through crater rim sections augmented the light microscope macroviews, and allowed specific microstructural phenomena associated with crater-related flow to be unambiguously identified for the first time.

2. Experimental procedure

A 5 mm light gas gun was utilized in impacting 3.18 mm spheres of either 1100 aluminium ($\rho = 2.7\ g\ cm^{-3}$) or soda–lime glass ($\rho = 2.2\ g\ cm^{-3}$) against OFHC (99.98%) copper target plates ($\rho = 8.9\ g\ cm^{-3}$) at hypervelocity ($u_o > 5\ km\ s^{-1}$). Two different copper target plates were impacted. That impacted by the aluminium projectile was 1.3 cm thick in the mill-processed condition. It had an average, real grain size of 38 μm determined by multiplying the mean intercept length by 1.5 [19]. The grain-size measurements included twin boundaries. In the mill-processed condition this target plate also had a dislocation density determined to be roughly $10^{10}\ cm^{-2}$ using the intercept method of Ham, and correcting for the invisible fraction of dislocations for operating reflections of $g = \langle 1\,1\,1 \rangle$ for grain-surface orientations of (1 1 0) observed in representative thin sections in the transmission electron microscope [20]. The second plate had a thickness of 2 cm and was annealed from a mill-processed condition for 10 h at 1000 °C. This produced a real grain size of 763 μm and an average dislocation density of about $10^9\ cm^{-2}$ [20]. These starting target plate microstructures are illustrated typically in Fig. 1.

Table I summarizes the two hypervelocity impact examples, including the resulting crater geometries and geometrical ratios. Table I also summarizes the associated impact velocities and corresponding pressure calculations. The two pressures noted represent the so-called planar impact approximation, or the shock Hugoniot pressure, P_s, calculated at the point of impact [8, 19], and the pressure associated with the hydrodynamic approximation of cratering, or the Bernoulli pressure, P_B. The corresponding, average, Vickers' microhardness numbers (VHN) are also listed in Table I.

The craters in each target plate were cut to reveal one exact half-section and a corresponding section. The exact half-sections were used to measure the crater geometries (Table I) and were polished to a 0.3 μm aluminium oxide powder slurry finish, etched, and examined by light metallography. A series of overlapping photographs were taken of the smaller crater in

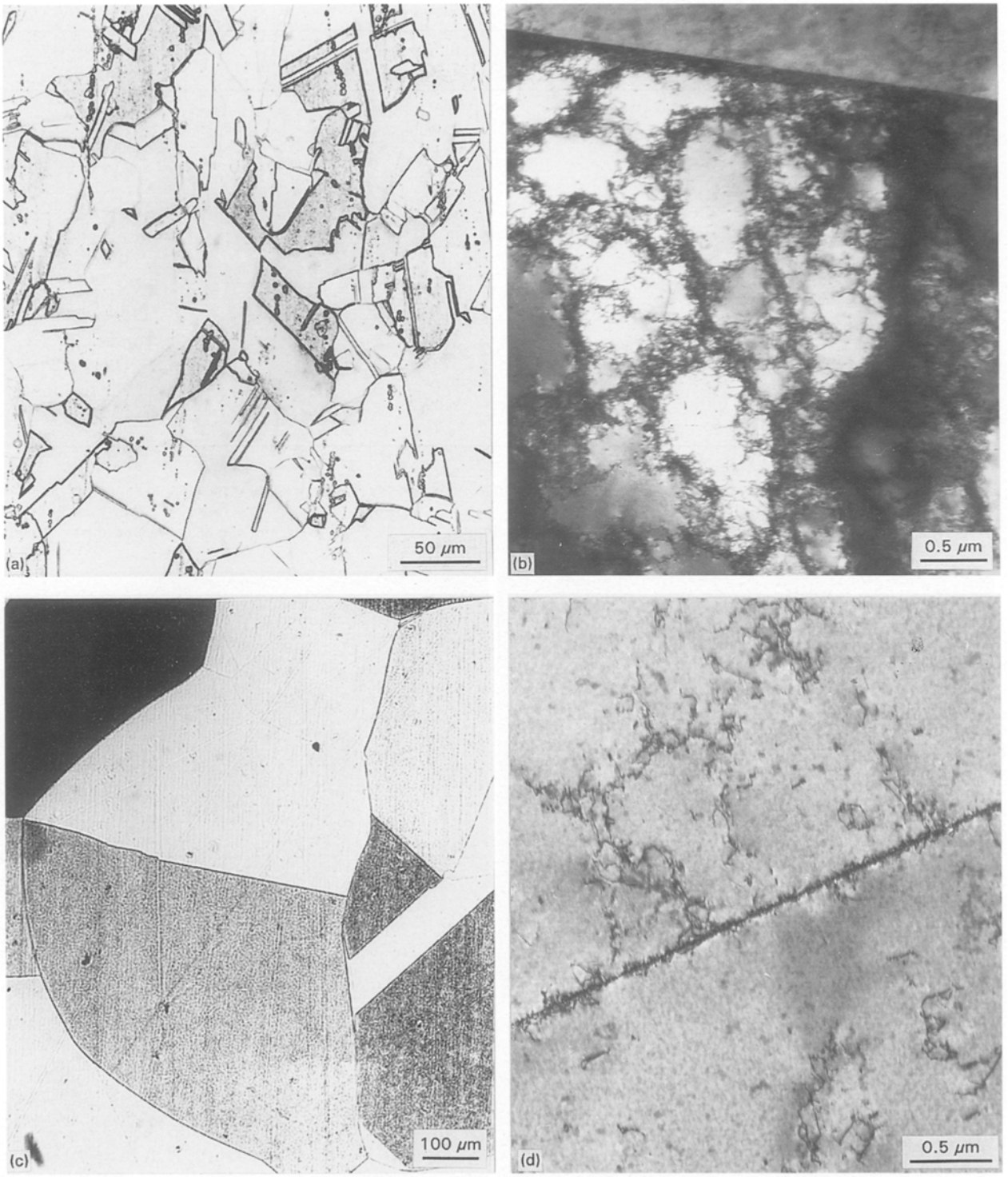

Figure 1 Initial copper target microstructures. (a) Light microscope view of the grain structure in a mill-processed target. (b) TEM image typical of microstructure in (a), showing dislocation cells. (c) Light microscope view of large-grained annealed target. (d) TEM image typical of microstructure in (c), showing remnant dislocations, near a coherent twin boundary.

the harder target plate at $\times 150$ while the larger crater in the softer target plate (Table I) was photographed at $\times 50$ or $\times 100$. A series of photographs was also made for each crater extending from the crater wall a distance of roughly 8 mm along the impact axis. Enlarged views were also made of the rim sections for each crater, and selected rim samples were extracted from the half-sections and examined in a scanning electron microscope to observe the fracture features at their perimeters. Larger rim sections which could be extracted from the larger crater in the softer target (Table I) were ground and polished in the plane of the rim and modified 3 mm discs were prepared by dimpling and electropolishing these discs to electron transparency using a Struers Tenupol-3 electropolisher. Representative discs were also prepared from sections extracted along the impact axis and extending from the crater bottoms as demonstrated previously by Rivas *et al.* [21]. Electron transparent thin sections were therefore prepared from sections extracted both parallel to the half-section plane and perpendicular to this plane (perpendicular to the direction of impact

TABLE I Experimental, hypervelocity impact conditions for OFHC copper targets

Parameter/property	Mill-processed (MP) target plate	Annealed (A) target plate
Plate thickness (cm)	1.3	2.0
Impacting paticle and density ($g\,cm^{-3}$)	1100 aluminium (2.7)	Soda–lime glass (2.2)
Impacting particle diameter, d_p (cm)	0.32	0.32
Impact velocity ($km\,s^{-1}$)	6.01	5.83
Impacting particle density/ target density (ρ_p/ρ_t)	0.30	0.25
$\rho_p\rho_t$	24.03	19.58
Real average grain size (μm)	38	763
Dislocation density, ρ (cm^{-2})	$\sim 10^{10}$	$\sim 10^{9}$
Average Vickers' hardness (VHN)[a]	82	67
Hugoniot (shock) pressure, P_S(GPa)[b]	118	108
Bernoulli pressure, P_B(GPa)[c]	20	18
Crater depth, p(cm)	0.35	0.46
Crater diameter, D_c(cm)	0.94	1.01
p/D_c	0.38	0.45
p/d_p	1.09	1.44
D_c/d_p	2.94	3.19

[a] Vickers' microhardness measured with 200 gf load.
[b] $P_s = \rho_t(C_t + S_tU_{pm})\,U_{pm}$, where ρ_t is the target density, C_t is the bulk sound velocity, S_t is a material constant, and U_{pm} is the modified projectile velocity in the compressed region after impact [7, 18].
[c] $P_B = [\rho_p\rho_t/(\rho_p^{1/2} + \rho_t^{1/2})^2]u_o^2/2$, where ρ_p and ρ_t are the projectile and target densities, respectively, and u_o is the projectile impact velocity.

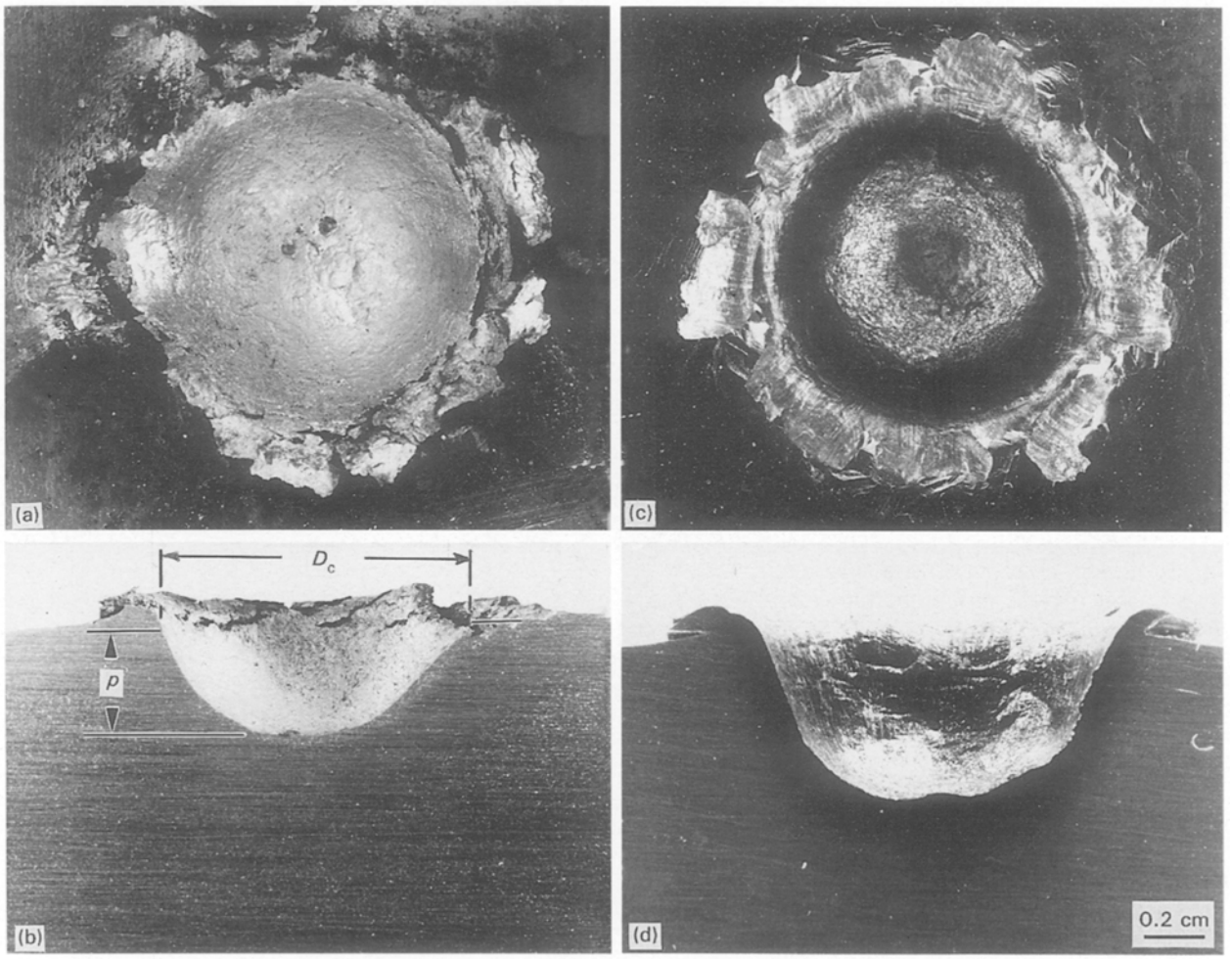

Figure 2 Plane (normal) views and corresponding cross-section views of experimental craters in experimental copper targets. (a, b) Impact crater in mill-processed small-grained (38 μm) target for a 1100 aluminium projectile velocity of 6.01 $km\,s^{-1}$. (c, d) Impact crater in annealed large-grained (763 μm) target for a soda–lime glass projectile velocity of 5.83 $km\,s^{-1}$. The convention for measuring the crater geometry is noted in (b).

below the crater wall and tangent to the crater wall radius). A Hitachi H-8000 STEM operated in the conventional TEM mode (at 200 kV operating potential and employing a double-tilt stage) was used to examine the electron transparent thin sections.

3. Results and discussion

3.1. Crater microstructure observations

Fig. 2 shows the two crater examples summarized in the experimental crater data listings in Table I. The methodology (or convention) for measuring the crater

dimensions is illustrated in Fig. 2b. Fig. 2 illustrates a distinctly different cratering behaviour for the annealed (A) target in contrast to the mill-processed (MP) target; consistent with the measurements shown for comparison in Table I (compare Fig. 2a and b with c and d). It is interesting to note that although the aluminium projectile density and impact velocity are slightly larger for the mill-processed hardened target (VHN = 82) in contrast to the soda–lime projectile density for the softer (annealed) target (VHN = 67), the softer target exhibits a considerably larger crater (comparing the depth of penetration, p, and the diameter, D_c, in Table I). This is due in large part to the considerable hardness difference, described previously by Ferreyra *et al.* [18]. It should also be noted in Fig. 2a that a "melt-solidified" film of the aluminium projectile coats the crater interior, while the crater in Fig. 2c, formed by the soda–lime glass projectile, is "clean".

There was also no evidence for projectile material impregnated into the base of either crater. This feature is apparent from the magnified light microscope views of the etched crater cross-sections shown in Fig. 3, particularly Fig. 3c and d. Fig. 3 also illustrates quite different crater-related microstructural features in these two structurally different targets. Despite the fact that fine microstructure in the photographic composites in Fig. 3 are not easily resolvable, there is no evidence for melt of melt-related (solidification) microstructures adjacent to the crater walls. There are considerably more grain distortion and related plastic deformation features associated with the mill-processed target in Fig. 3d in contrast to the much larger grained annealed target in Fig. 3c. The general flow-like features of the microstructure adjacent to the crater walls suggests severe plastic flow from the crater floor upward into the rim area (Fig. 3b). This region of extreme plastic deformation evolves into a less severely distorted grain structure with the emergence of linear microstructural features. These are interspersed in the deformed grains, and become dominant especially a few millimetres from the crater floor. There also seems to be a preponderance of microbands along the crater wall and rim-related regions in the large-grained (annealed) crater in contrast to the smaller grained (mill-processed) crater. These features are illustrated on comparing Figs 4 and 5 which are magnified views at the arrowed regions (r) in Fig. 3a and b, respectively.

These microstructural features are more readily apparent in magnified strips along the impact axes from the base of both craters, shown for comparison in Figs 6 and 7. Both Figs 6 and 7 illustrate a narrow zone (I) characterized by dynamic recrystallization as described in previous observations [1–3], a transition zone (TR) composed of deformed grains (which is more uniform and identifiable in Fig. 6), and an intermixing of linear features, and a zone (II) of linear features; previously identified as microbands [1–3]. Beyond the microband zone, the microstructure gradually evolves into the base microstructure. This is particularly notable in Fig. 7 which shows discontinuous zones extending further from the crater wall than in the corresponding microstructure strip in Fig. 6, which is continuous from the crater wall. Beyond the linear deformation band or microband features, there is some evidence for deformation microstructures within the grains, but there is not much grain distortion. In fact, there is effectively no grain distortion in zone II in Fig. 6. This feature is generally true also for the annealed, large-grained crater but it is difficult to see this from Fig. 7 because of the very large grain size and the different etching characteristics.

Fig. 8 shows the microstructural details in Fig. 7 as observed in the TEM. Dynamic recrystallization, with very small grains having simple misorientation angles in excess of about 10°, dominates the region adjacent to the crater wall (Fig. 8a). Moving outward from this narrow zone (extending out roughly 0.2 mm from the crater wall as shown in Fig. 3c), the microstructure is dominated by dislocation cells having small sizes (<1 μm measured between cell centres) and thick walls, some elongated dislocation cells, sub-grains (with misorientations of 2°–5°), and linear features or microbands as shown in Fig. 8b. Beyond zone II (Figs 6 and 7), which is dominated by linear deformation structures or microbands extending as far as 4–6 mm from the crater bottom, dislocation cell structure dominates, and increases in cell size and decreases in cell wall width (and dislocation density) with distance from the crater, as shown in Fig. 8c and d. This zone extends to more than one crater diameter in the annealed (A) target (or about 15 mm from the crater floor) and about 8 mm in the mill-processed, small-grain target). Note that Fig. 8c and d are in contrast to essentially no dislocation cells in the starting target plate (Fig. 1d).

The linear deformation features in zone II (Figs 6 and 7) are of particular interest. In prior studies of mill-processed target material, they have been uniformly characterized as microbands, with no deformation twin features (including no twin reflections in selected-area electron diffraction patterns) [1–3, 21–23]. These microband features are observed for the mill-processed target in this study as well (Figs 6 and 9b). The linear features in the annealed target (Figs 7 and 8b) in zone II, etc., are also microbands, often extending as intermixed bundles which fill the whole or portions of these large grains as shown in Fig. 4. These features are shown in Fig. 9 which compares not only prominent etched microstructural features in the optical metallograph views (Fig. 9a and c), but also in the corresponding TEM images (Fig. 9b and d). While the image features are not so readily discernable in the light microscope views (Fig. 9a and c), the TEM views in Fig. 9b and d show the irregular (wavy) and even lenticular nature of some microbands in the mill-processed small-grain size target (Fig. 9b). They become somewhat more dense bundles, often more elongated and continuous cell-like features in the annealed target (Fig. 9c). The misorientations and the sizes (widths) of microbands vary over a range of 1°–4° and 0.1–0.4 μm, respectively. The misorientation is specifically notable in the selected-area diffraction (SAD) pattern inserted into Fig. 9b (arrowed).

It should be noted that in the TEM views in Fig. 9b and d the microbands are not only unidirectional, but coincident with traces of a single set of {1 1 1} (slip)

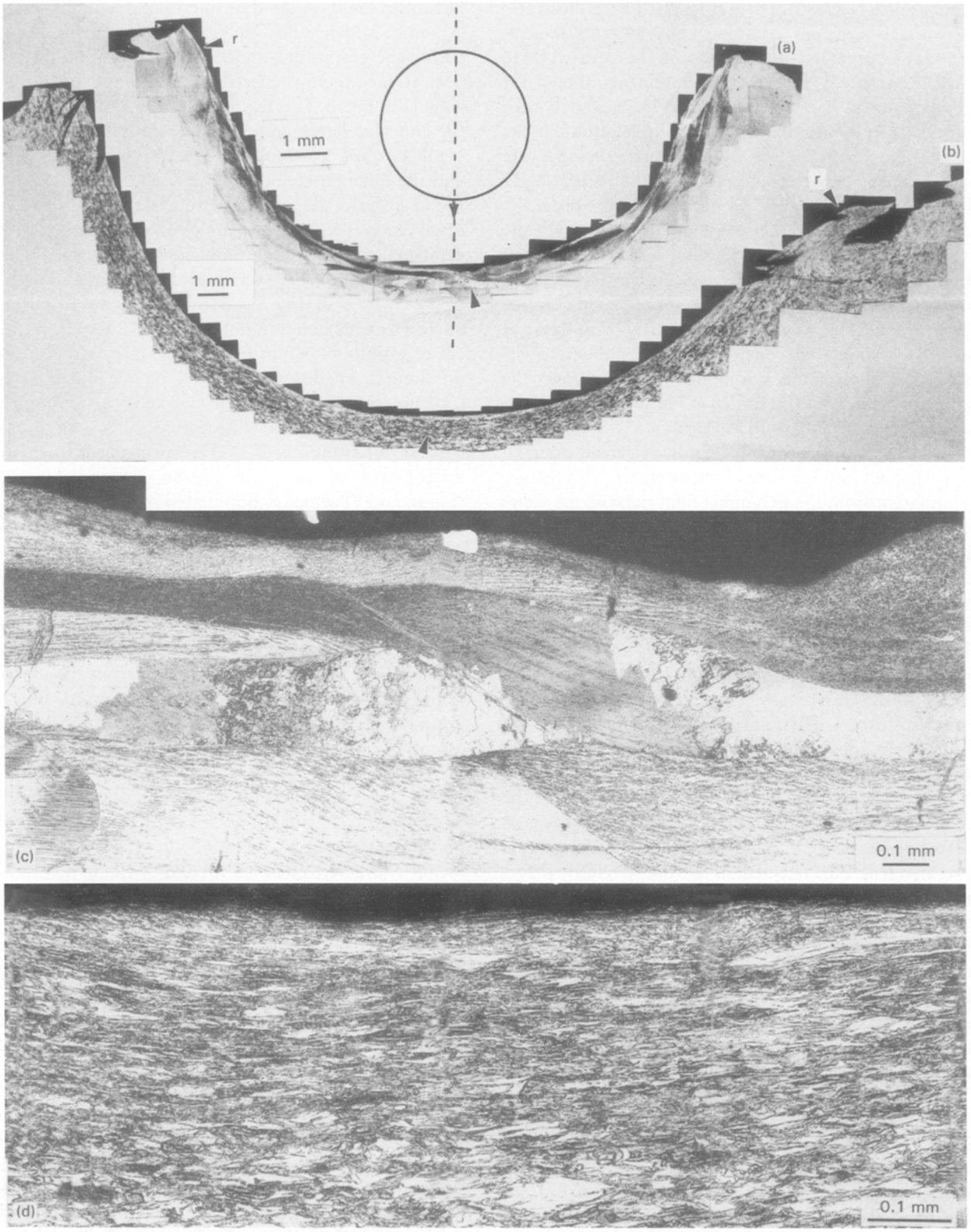

Figure 3 Reduced reproduction of cross-section composite views for the craters shown in Fig. 2. A scaled, schematic view of the spherical impact projectile is shown on the corresponding impact axis (dotted) for (a). (a) The crater in the annealed target (Fig. 2d); (b) the crater in the mill-processed target (Fig. 2b). Note the magnification differences (markers) for these two composite views. (c) An enlarged view of the region marked with an arrow at the crater base in (a); (d) an enlarged view of the region marked with a corresponding arrow in the crater base in (b).

planes. Also, while there seems to be a preponderance of examples where the microbands are coincident with traces of one primary set of {1 1 1} planes which are perpendicular to the specimen surface, such as the situation shown in Fig. 9, there have been numerous observations of microbands coincident with other primary {1 1 1} planes as well, which make some angle with a specific grain-surface orientation. These features are in contrast to shock-induced deformation twins which are often observed in all possible (non-coplanar) {1 1 1} slip trace directions for specific grain-surface orientations [24, 25].

Figure 4 Enlarged view of the crater wall/rim-related region in the large-grained (annealed) crater marked with the arrow at "r" in Fig. 3a. Note the propensity of microbands in many grains.

Fig. 10 shows comparative views of a unique and identical crystallographic zone axis ([1 1 0]) which allows the microbands and deformation twins to be unambiguously differentiated. In Fig. 10a, microbands along [1 $\bar{1}$ 2] (indicated by the arrow in the image) produce no (extra) twin reflections in the SAD pattern insert. In Fig. 10b, deformation twins in an obliquely shock-loaded copper rod having a grain size about half the large grain size of the annealed target (375 μm) [24], and lying along [1 $\bar{1}$ 2] (arrowed in the image), produce twin reflections and reflection rows perpendicular to this twin trace direction. These twin

Figure 5 Enlarged view of the crater wall/rim-related region in the small-grained (mill-processed) crater marked with the arrow at "r" to the right in Fig. 3b.

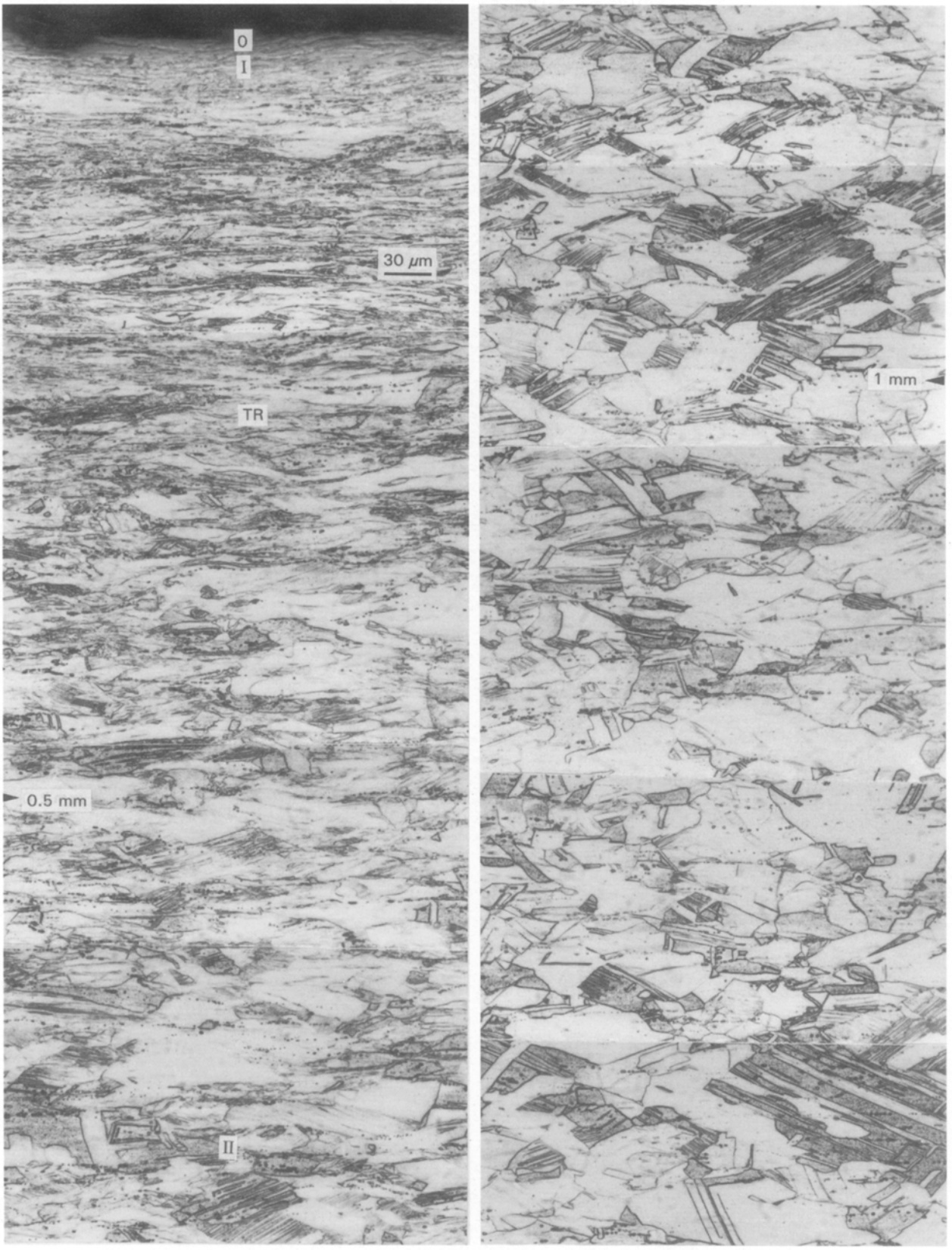

Figure 6 Light microscope view of the microstructure corresponding to a narrow strip along the impact axis shown in Fig. 3d, at distances noted from the crater wall (at zero) for the 6.01 km s^{-1} crater in the mill-processed target (Fig. 3b). The distance increases continuously from the left to right strip. Prominent microstructural zones are indicated.

reflection rows are perpendicular to the $\{\bar{1}\,1\,1\}$ twin planes, corresponding to extra reflections at $\langle 1\,1\,1\rangle/3$ [20, 22, 23]; unambiguously distinguishing these linear microstructure features from the microbands in Fig. 10a. There have been no observations of deformation twins associated with either crater in these extreme target conditions (Figs 6 and 7), examined in this investigation. Microbands intermixed in a preponderance of deformation twins have been observed recently for the oblique shock loading of copper rods with different grain sizes [24]. This intermixing is not shown in the results reproduced in Fig. 10b. In this

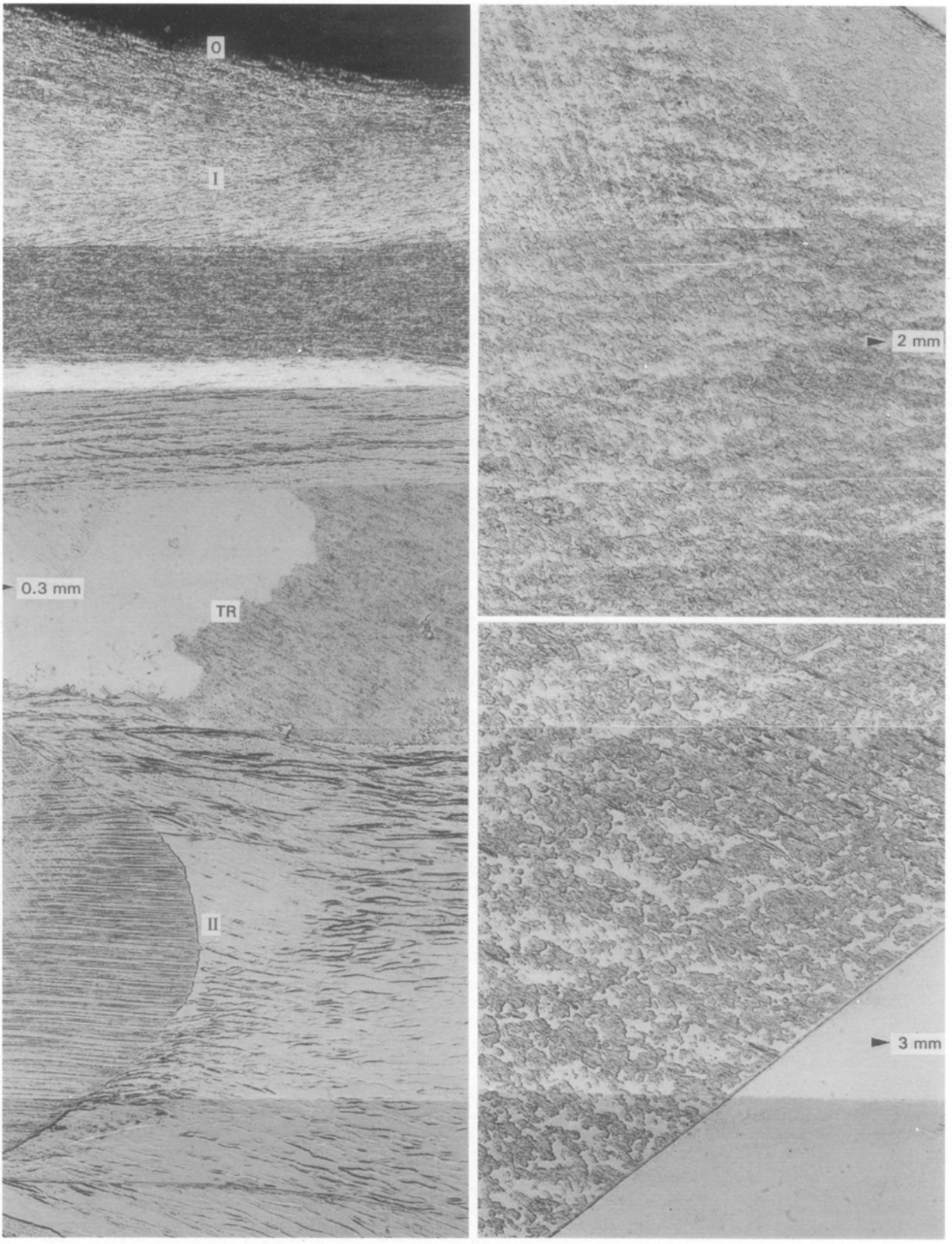

Figure 7 Light microscope view of the microstructure corresponding to a narrow strip along the impact axis shown in Fig. 3c, at distances noted from the crater wall (at zero) for the 5.83 km s^{-1} crater in the annealed target (Fig. 3a). The distance increases discontinuously from the left to right strip. Prominent microstructural zones are indicated together with approximate distances from the crater bottom. Magnification in Fig. 7 is the same as shown in Fig. 6.

work by Sanchez *et al.* [24], the propensity of deformation twins increased with increasing grain size in a grain size range of 29–375 μm. The corresponding Vickers' hardness for this range of grain sizes prior to shock loading ranged from 60–55 VHN, respectively. This observation is consistent with other earlier observations of twinning in plane-wave, shock-loaded metals and alloys [25], and more recent observations by Meyers *et al.* [26] for plane-wave shocked copper. It was not obvious in the work of Sanchez *et al.* [24]

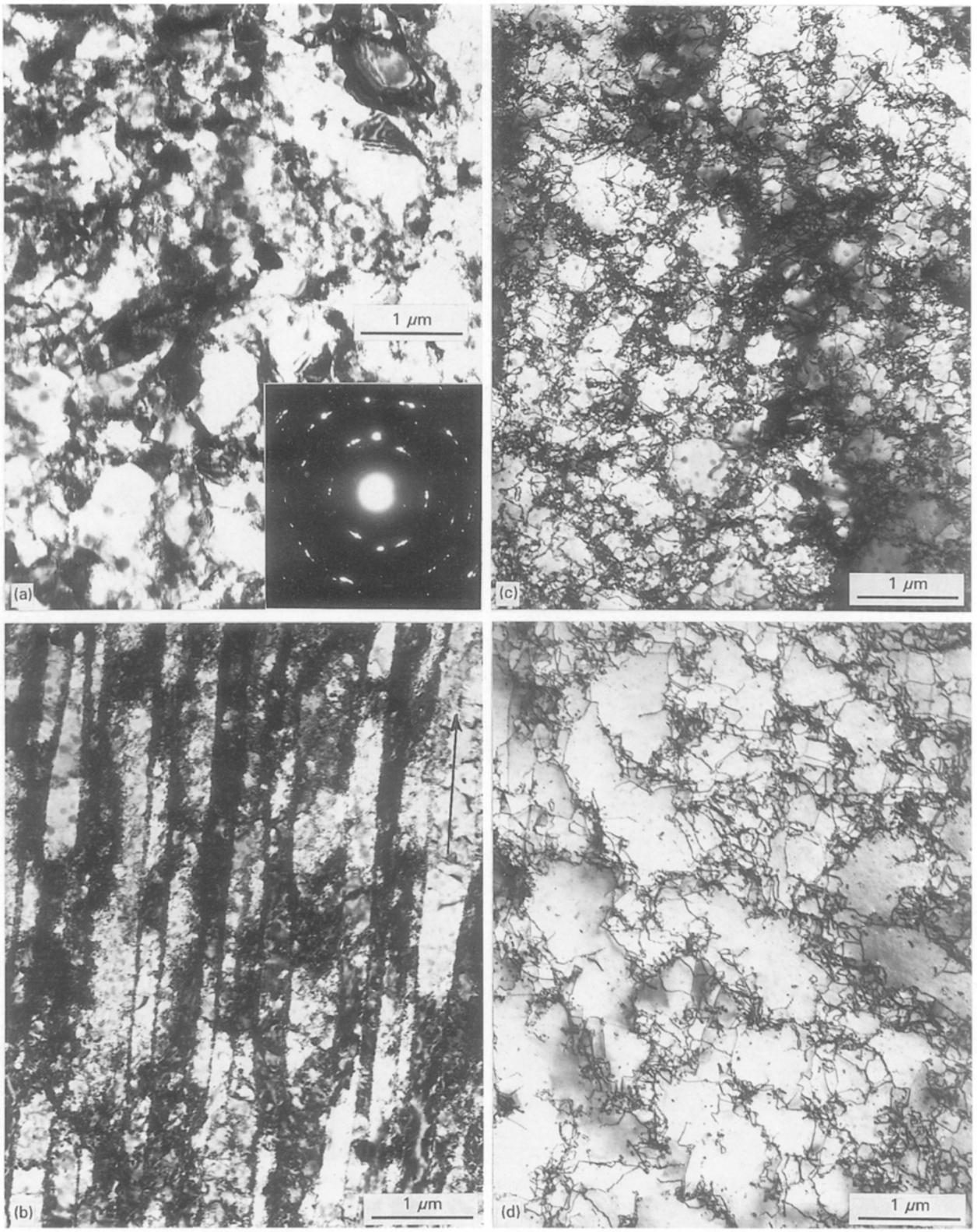

Figure 8 TEM bright-field image sequence showing evolutionary microstructures extending from the annealed, large-grained crater wall. (a) Small, dynamically recrystallized grains near the crater wall (~0.1 mm). The SAD insert shows the average misorientations ~10°. (b) Microbands in a (1 1 0) oriented grain which are coincident with traces of $\{\bar{1}\,1\,1\}$ planes shown by the arrow (~12 mm). (c) Small dislocation cells beyond the microband zone at roughly 12 mm from the crater bottom. (d) Evolving dislocation cell structure (increasing cell diameter) at roughly 14 mm from the crater bottom.

whether there was a corresponding variation of microband density with grain size. However, the twin density decreased significantly as the grain size was reduced, consistent with recent observations of Meyers *et al.* [26].

It is apparent that the significant differences between the two targets in this study are related to the starting microstructure, and the resulting initial hardness, because the shock geometry is the same, and the shock pressure is actually larger in the smaller grained target cratering example than the large-grained target example. Also, while a variation in grain size in the work of Sanchez *et al.* [24] did not eliminate deformation twins completely or seem appreciably to influence

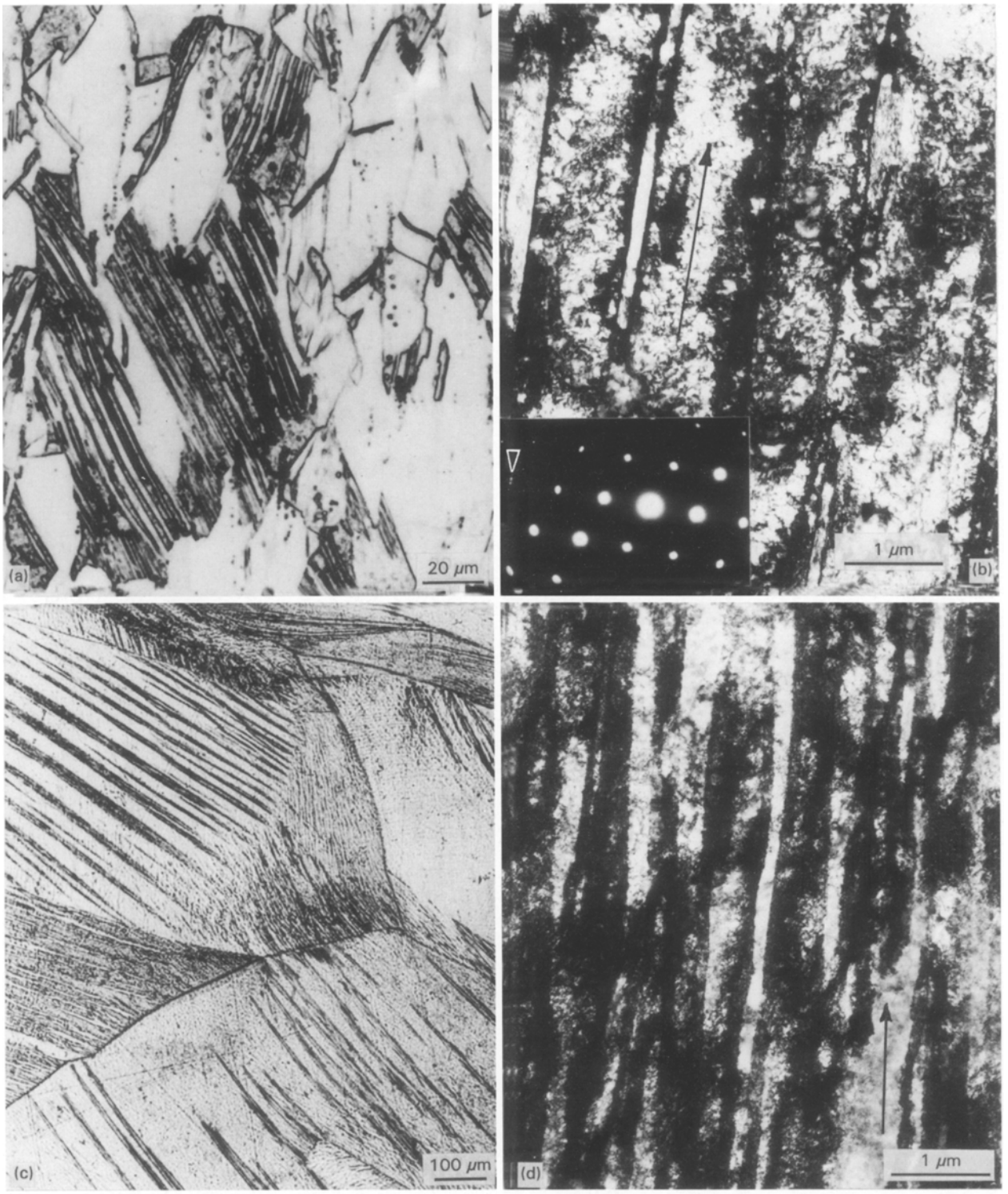

Figure 9 Light microscope and TEM comparisons of microbands in Zone II of the mill-processed crater-related target area (Fig. 6), (a, b) respectively, and in Zone II of the annealed, crater-related target area (Fig. 7), (c, d), respectively. In both (b) and (d) the grain surface orientations were (1 1 0). The microbands are coincident with traces of $\{\bar{1}\,1\,1\}$ planes as indicated by the arrows. The SAD pattern insert in (b) illustrates these crystallographic features. In addition, the SAD pattern in (b) also shows no twin-related reflections, but the misorientation of the microbands is apparent by the matrix reflection splitting noted specifically at higher order reflections indicated by the arrow.

the microband density, it did not appear that the microbands were restricted by grain size in the same way that deformation twins are restricted. However, on comparing the occurrence of microbands in the mill-processed (MP) and annealed (A) target craters, there seems to be a recognizable propensity of microbands associated with the larger grained annealed target crater than the mill-processed and smaller grained target crater. These features are especially obvious on comparing the enlarged crater wall sections shown in Figs 4 and 5, and especially the comparative TEM views of microbands shown in Fig. 9b and d.

It would seem logical that because the microbands and twins are both coincident with $\{1\,1\,1\}$ trace directions in specific crystallographic (grain) orientations and apparently influenced in the same way by grain size, there is some connection between the shear-related twinning mechanism and the mechanism of

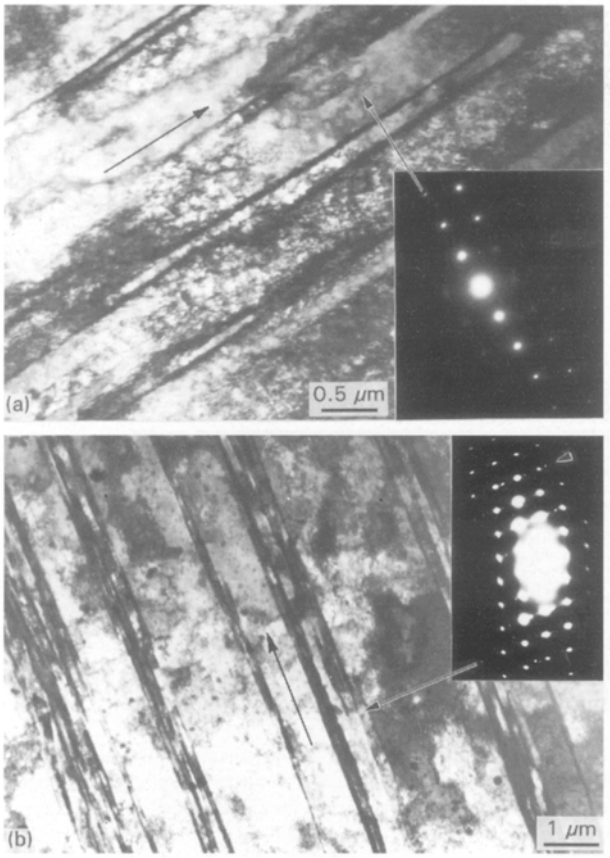

Figure 10 TEM bright-field comparison of microbands (a) below the crater in the mill-annealed target compared with deformation twins (b) in cylindrically (oblique) shocked copper. The SAD pattern inserts show identical [1 1 0] zone axes, and [1 $\bar{1}$ 2] trace directions coincident with {$\bar{1}$ 1 1} at 90° to the (1 1 0) grain surface. This trace is indicated by the arrow in the image which is perpendicular to the ⟨1 1 1⟩ directions shown extending from the SAD patterns. The corresponding operating reflections are $\boldsymbol{g} = \langle 1\,1\,1\rangle$. Twin reflections for ⟨1 1 1⟩/3, perpendicular to the deformation twin traces along [1 $\bar{1}$ 2] are shown in the SAD pattern of (b). The small arrow in the SAD pattern in (b) shows a row of matrix and twin reflections. (b) Courtesy of J. C. Sanchez [24] from work reported therein.

microband formation in shock-wave deformed copper. However, the exact nature of such a mechanistic relationship is currently not clear. Microbands have been reported in numerous fcc and bcc metals and alloys [27, 28], and Huang and Gray [28] have recently discussed a dislocation double-wall mechanism for microband formation. However, they did not suggest any specific relationships between microbands and deformation twins, and their discussion does not offer any clear insight into resolving the current observations, especially in terms of specific dislocation or micro-shear mechanisms.

3.2. Rim microstructures

While there is some microbanding (especially in the large-grained target) associated with the upper portions of the corresponding craters (Fig. 3), this zone (zone II in Figs 6 and 7) is not spherically symmetrical. It extends further from the crater wall in a region below the craters as compared with the upper crater regions. These features are especially apparent in the rim region where there is less evidence for microbanding than in regions near the crater bottom, including zones on either side of the impact axis. Fig. 11 shows enlarged views of crater-rim cross-sections for the two experimental craters. The heavily deformed plastic-flow microstructures near the crater wall (Fig. 3c and d), and characterized by dynamic recrystallization, dominate the upper rim microstructure (Figs 4 and 5). The lower rim portion connected to the target is characterized by relatively undistorted (but occasionally microbanded) grains which have been up-lifted as the crater formed, and material jetted plastically out of the crater region (compare with Figs 4 and 5). There is no evidence of either melt or melt-related solidification structures anywhere in the rim cross-sections. The rim edge in the mill-processed target (Fig. 11b) shows extensive fracture corresponding to only partial necking. The upper rim region near the edge in Fig. 11b exhibits considerable void formation associated with extensive cracking and rim fracture. These features are absent in Fig. 11a.

While there are some similarities in the rim cross-section microstructures associated with the large-grained target crater (Fig. 11a) in contrast to those of the smaller grained target crater (Fig. 11b), there are some very notable differences which are apparent on comparing Fig. 11a with b. Fig. 11a shows a comparatively larger rim, consistent with a somewhat larger crater in a considerably softer, more ductile, and more plastic target. In addition, there are only a few examples of microbands (arrows) in the undistorted and up-lifted grains of the target. The rim edge is more classically necked in Fig. 11a, and there is a very fine recrystallized grain size in the upper rim plastic flow zone or multiple zones, which flow independently over a width of recrystallized grains. There is also evidence of extensive and continuous shear band-like features separating the plastic-flow (recrystallized) layers or zones in the upper rim section. These extensive flow zones are greatly reduced in the mill-processed target crater rim. Unlike the smaller grain-related rim cross-section in Fig. 11b, Fig. 11a shows no evidence for void formation.

The specific features of the fine recrystallized grain structure in the upper rim regime are illustrated in the magnified cross-sectional light microscope image shown in Fig. 12a and the in-plane rim TEM images shown in Fig. 12b–d. The SAD pattern inserts in Fig. 12b and d also confirm the large misorientations for the recrystallized grain structure previously illustrated in Fig. 8a. The ratio of initial target grain size (763 μm) to the plastically jetted rim grain size (~0.5 μm in Fig. 12b and c), D_o/D_s, is about three orders of magnitude. This is about an order of magnitude greater than the recrystallization features observed for shaped charge jets [15], and characteristic of dynamic recrystallization.

Fig. 13 shows, for comparison, the fracture surfaces for the two rim edges shown in Fig. 11a and b, respectively, for the large-grained and small-grained targets. The SEM images show the differences in necking efficiency for the jetting rims, and the mechanics of rim formation for these two different targets. There is considerably more porosity in the small-grained target crater (Fig. 13c and d) in contrast to the large-grained

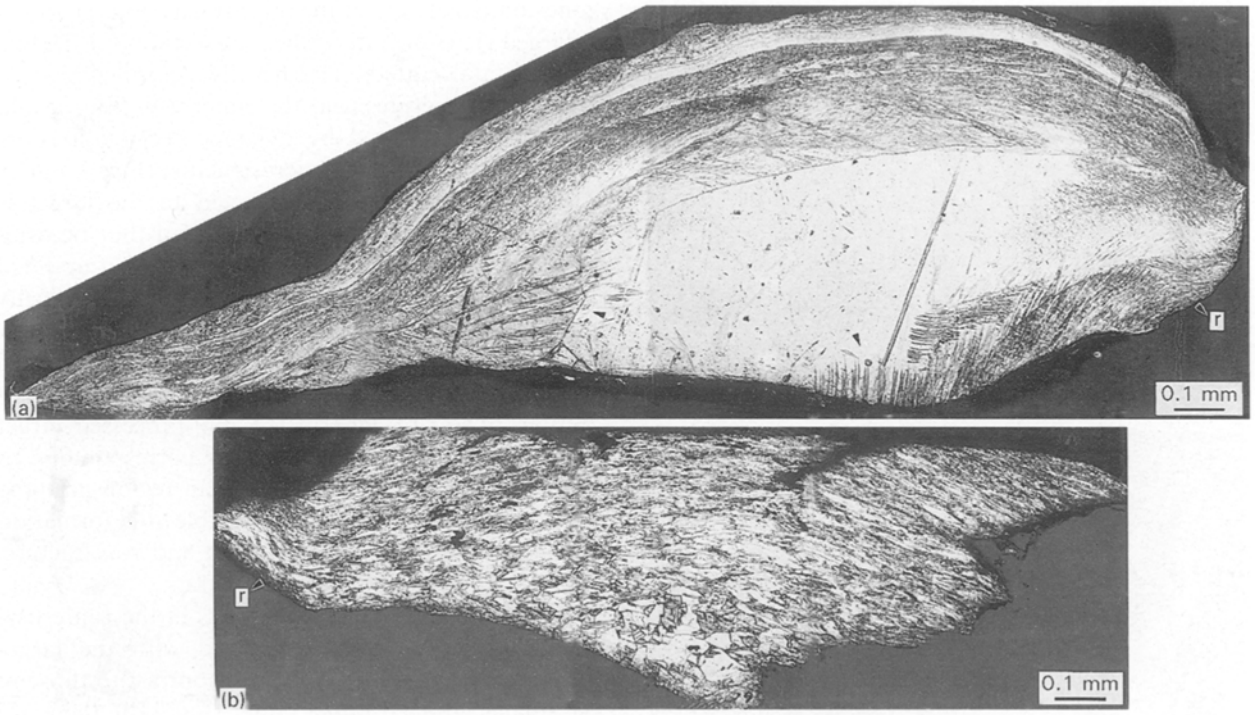

Figure 11 (a) Magnified (LM) view of extracted crater rim section (edge view) for the annealed target crater (corresponding to an impact velocity, $u_o = 5.83\ km\,s^{-1}$). (b) Magnified (LM) view of crater rim (edge view) for the mill-processed target crater (corresponding to an impact velocity, $u_o = 6.01\ km\,s^{-1}$). Note the correspondingly detached rim segments for (a) and (b) marked (r) to the right and left of the craters in Fig. 3a and b, respectively. Arrows in (a) show prominent microbands. Also note that (a) and (b) correspond to the rim regions illustrated in connection with crater wall flow in Figs 4 and 5, respectively.

target crater (Fig. 13a and b) due in part to the microstructure differences in the targets, and the correspondingly different (plastic) flow phenomena. The annealed target crater forms an extremely necked region with a very thin fracture surface after particulation, as shown in Fig. 13a.

3.3. A model for hypervelocity impact cratering in metal targets

There are several microstructural similarities and differences which are readily recognizable in examining and comparing the hypervelocity impact craters (and crater section views) shown in Figs 3–12. The most apparent similarity involves the absence of any melt feature at or near the crater wall. A common microstructural feature is the narrow zone of dynamically recrystallized material extending from, and characterizing, the crater wall. This zone is slightly better defined in the mill-processed target crater bottom and side regions (Figs 3d, 6, etc.), but it becomes especially well-defined in the crater rim region where severe plastic jetting occurs (Figs 4, 5,11a). The fact that this phenomenon is related to stored energy of deformation, as recently proposed for shaped charges by Murr *et al.* [15], is perhaps implicit in differences in the zone of recrystallized material in the annealed target ($D = 763\ \mu m$) in contrast to such a zone in the mill-processed target ($D = 38\ \mu m$) where the hardness reflects a significantly greater degree of stored energy of deformation (67 VHN versus 82 VHN, respectively). It might also be pointed out that similar recrystallization effects (a zone extending from the crater wall bottom) have been reported for high-energy laser-induced cratering in polycrystalline and single-crystalline iron targets by Hallouin *et al.* [29]. This work also produced a zone identified as "deformation twins" beyond the recrystallized zone which did not appear to have been unambiguously confirmed by selected-area electron diffraction, and may have included microbands, or in fact may have been completely characterized by microband formation. This confirms the fact that the crater formation process is governed fundamentally by the spherically generated shock wave, because no projectile is involved in laser-induced cratering. Here again, in the laser-induced cratering, there was no recognizable melt phenomena, and the crater rim formation, etc., were essentially the same as observed in this study.

The recognizable differences in this study (in possible contrast to the laser-induced craters in the work of Hallouin *et al.* [29]) involve the propensity for microband formation below the crater in contrast to deformation twins (or twin-faults). In addition, the target impacted with the aluminium alloy projectile (mill-processed harder target) produced a crater lined with melted and solidified projectile material which, in effect, formed a crater shell which ejected material at its perimeter like the actual target crater. By contrast, the crater in the annealed (softer) target did not exhibit any evidence of impacting projectile remnants. In about half of the craters observed on spacecraft structures, there is also no projectile residue. Consequently, either these projectiles completely melt and vaporize, or they are ejected by shock (spall) fragmentation, or more complex mechanisms involving fragmentation,

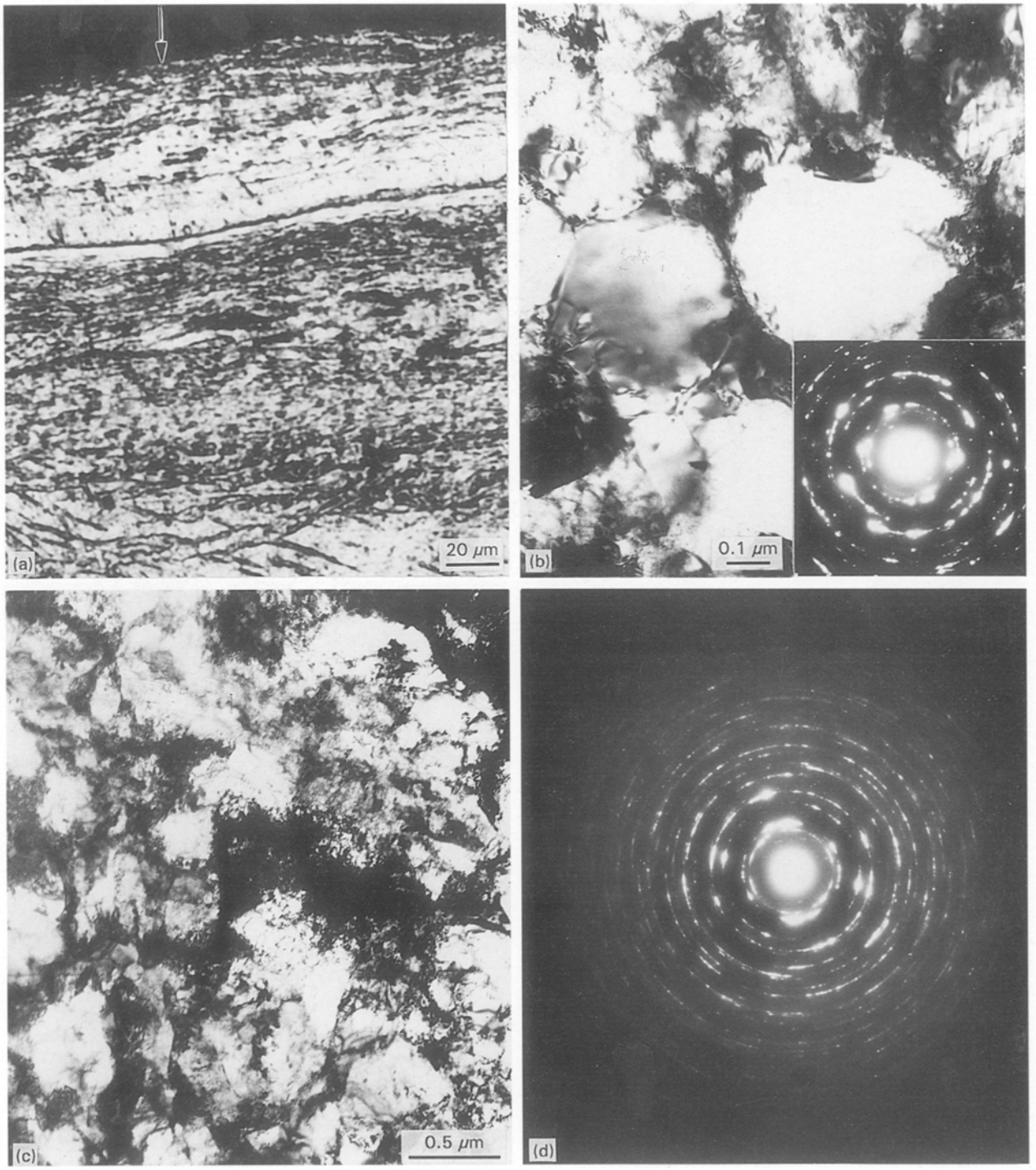

Figure 12 (a) Magnified (LM) view of rim-jet (extreme plastic flow) zone in Fig. 11a showing very small grain structure. (b) TEM view looking into the jetted rim surface or upper flow region; perpendicular to the view shown in (a) (in the plane perpendicular to the arrow in (a)). SAD pattern insert shows large misorientation angles indicative of dynamic recrystallization. (c, d) A similar region at lower TEM magnification. The extremely small grain size produces a polycrystaline ring pattern in (d).

melting and vaporization. Many craters contain large sections (or segments) of projectiles in their base, especially when the projectile is strong, ductile, and has a high melting point, and the impact velocity is below about 1 $km\,s^{-1}$ [30, 31]. Stainless steel projectiles against copper targets behave in this fashion, and at very low velocities ($< 1\ km\,s^{-1}$) the projectile is embedded completely in a same-sized crater ($d_p \cong D_c$) [32]. Bernhard and Hörz [30], and Hörz *et al.* [31] have, in fact, traced the behaviour of soda–lime glass impactors into 1100 aluminium targets over a range of velocities from 1–7 $km\,s^{-1}$. Below about 2 $km\,s^{-1}$, the glass projectile is comminuted and sheared as it enbeds into the target. At 2.2 $km\,s^{-1}$ melt appears, and above 2.5 $km\,s^{-1}$ mixtures of glass melt and comminuted debris start creeping up the crater wall. Above about 5.5 $km\,s^{-1}$, the entire impactor is molten and increasingly large fractions of this molten impactor film are ejected from the crater rim area. Small quantities of unmelted residues were even found at 7 $km\,s^{-1}$ within the craters.

At very high velocities ($> 8\ km\,s^{-1}$), it is generally assumed that projectiles essentially vaporize completely, and the final crater is primarily shaped by the

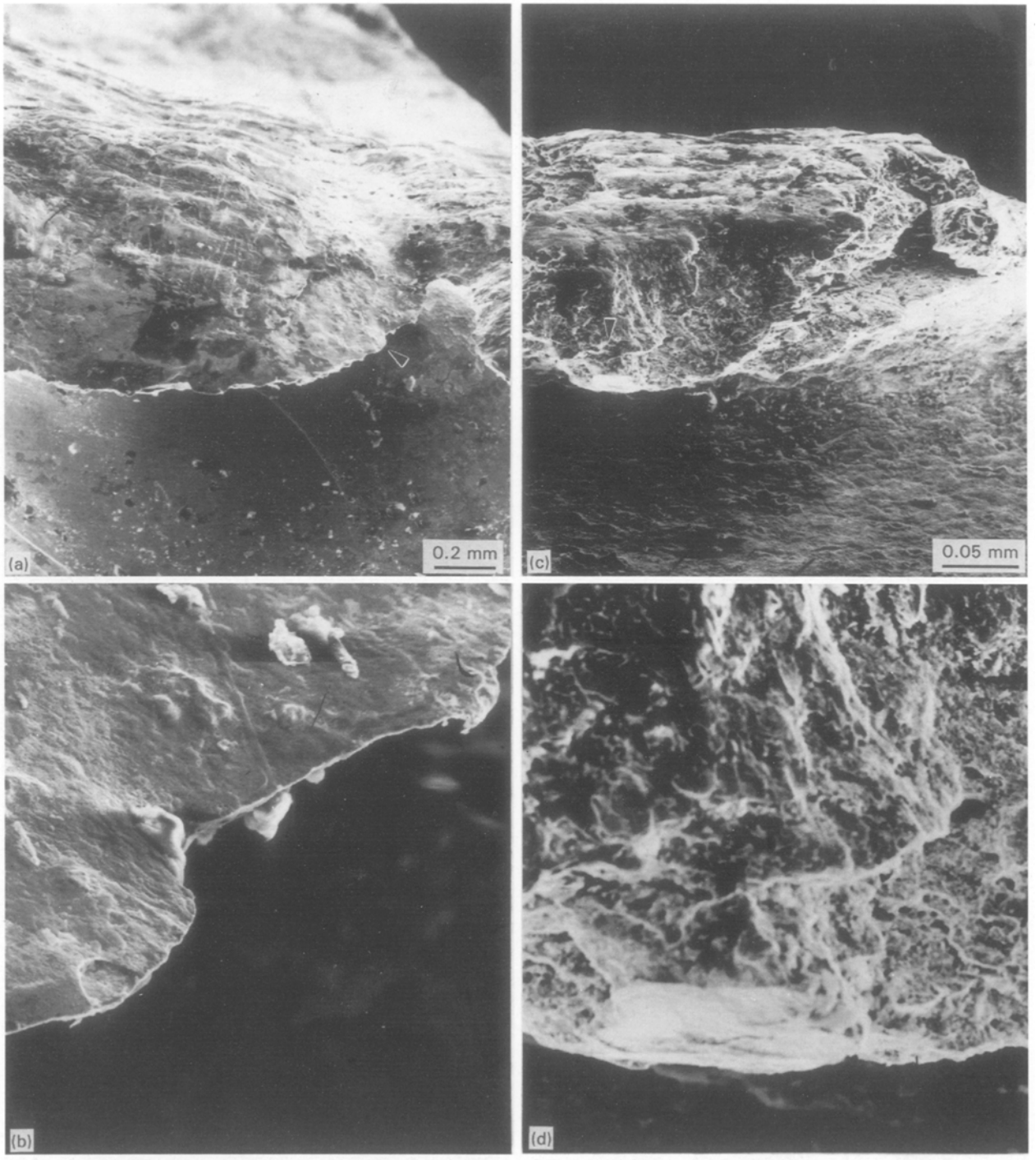

Figure 13 SEM views showing fracture features for the rim edges in both the annealed target crater (a,b), and the mill-processed target crater (c, d). The failed rim perimeter is ejected as a consequence of the crater jetting and failure. The rim failure in (a) and (c) differs as a consequence of differences in jetting and the tensile component.

shock wave. This feature is illustrated in contemporary computer hydrocodes, and an example is shown in Fig. 14 along with some comparative diagrams depicting the two crater conditions examined in this study.

A conspicuous feature of the computer-generated crater section view (Fig. 14c) is the absence of any microstructure-related damage characteristics well below the crater wall. The simulation illustrates only the deformation (strain) localization extending out from the crater wall in a narrow zone which scales (and extends) at a maximum $\sim 0.3\ D_c$. This is in contrast to the deformation observed below the annealed crater wall shown in Fig. 8d, for example, which extends as far as $\sim 1.5\ D_c$. However, the computer simulation does accurately depict the uplifting of the target to form the rim, and the general absence of deformation in the under side of the up-lifted, jetting rim as shown generally in Figs 4 and 5. The diagrams in Fig. 14a and b attempt to depict not only the current two experimental target conditions, but also the range of observations described for glass impactors into aluminium targets summarized above [30, 31]. However Fig. 14b may also be interpreted to depict the prospects that for very brittle projectiles striking relatively strong targets, there may also be some initial particle spallation and reduced melt. In addition, Fig. 14b

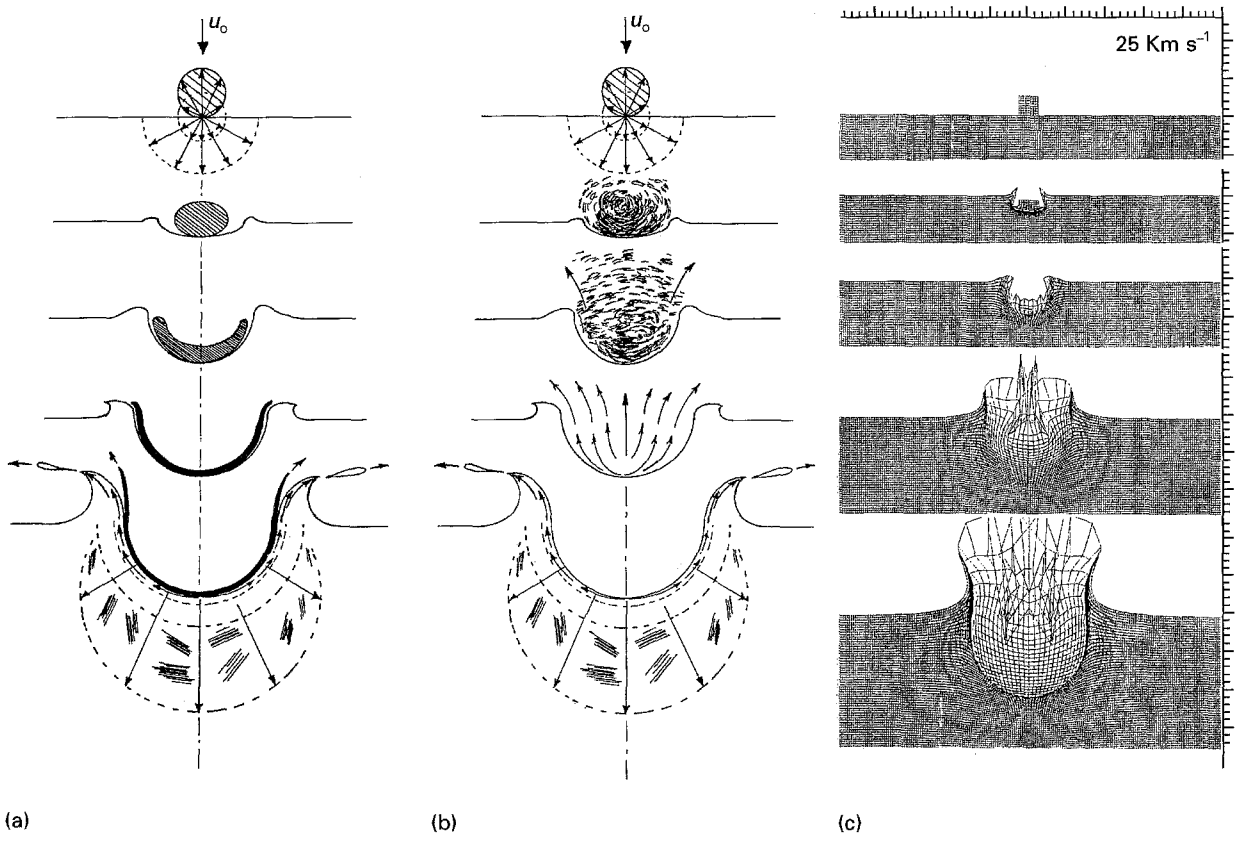

Figure 14 Schematic views for crater development in metal targets impacted by (a) ductile and (b) brittle projectiles, and (c) compared with a computer (hydrocode) simulation for a dense (iron) projectile striking an aluminium target at an impact velocity, $u_o = 25$ km s^{-1}, at different times after impact. In the computer simulation, the projectile vaporizes completely. In (a), the projectile is primarily melted against the crater wall, but there is no crater melt. In (b), the projectile is primarily ejected as shock-induced fragments together with melt and vaporized projectile material. Again, there is no crater-related melt, and the crater forms in the spherical shock-wave front.

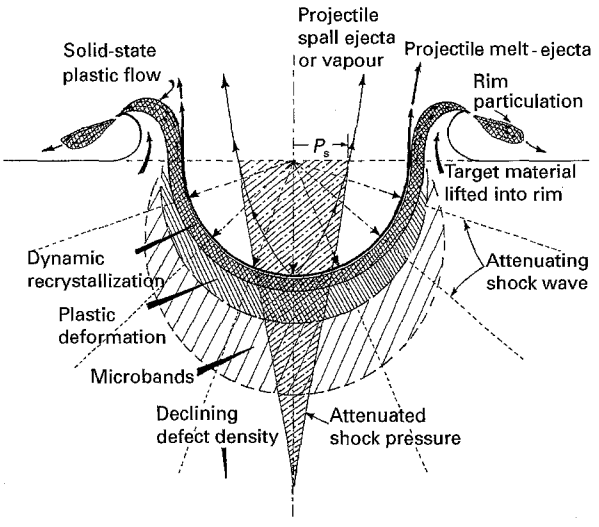

Figure 15 Schematic generalized crater formation and crater-related microstructure for copper targets examined in this study.

could also be interpreted to characterize significant projectile vaporization, especially for space impacts involving projectile velocities > 20 km s^{-1}. Indeed, depending upon the corresponding projectile and target hardnesses and strengths, as well as the impact velocities, the actual impact crater development in metal targets might involve a superposition of the diagrams in Fig. 14a and b.

Fig. 15 summarizes, graphically, a simple, phenomenological model of the craters (and only the craters) examined in this study, which may characterize craters in metal targets in general, if zone variations and specific microstructural issues are inserted or altered. The most important distinction depicted in contrast to geological cratering is the absence of crater wall-related melt/solidification phenomena, and the development of rim-jet particulation (and ejecta) by solid-state plastic flow. Indeed, a re-examination of cratering may reveal that there is considerably less melt-related phenomena in geological regimes than previously concluded. Furthermore, we have weighed these and other craters and measured the density of cratered regions only to find the same density and essentially no weight loss except for the particulation of the rims. Consequently, cratering in metals occurs by deformation-induced displacement and only the rim perimeters "eject" material by rim-jet particulation as a consequence of extreme tensile stress resolution and necking.

4. Conclusion

The most significant conclusion of this work is that there is no melt-related phenomena associated with hypervelocity impact crater formation in copper targets. Hypervelocity impact crater jetting in copper targets occurs primarily by extreme plastic flow, possibly a kind of superplastic phenomenon proposed for shaped charge jets by Chokshi and Meyers [17], or a related mechanism which manifests itself in dynamic

recrystallization and continuous shear-band development. As a consequence, crater rim jetting is fundamentally similar to jetting in metal-shaped charges such as copper, especially because the jetting-related regions and the crater wall exhibit dynamic recrystallization like copper-shaped charge jets.

The target microstructure and corresponding hardness play a significant role in the cratering process, and in establishing residual microstructural regimes. For example, dense microbands coincident with traces of {1 1 1} planes observed in the TEM were observed in a zone beyond the recrystallized grains, adjacent to the crater wall, and an intermixed zone of heavy plastic deformation. In addition, there were more microbands in the large-grained target crater than the small-grained mill-processed target crater. These observations seem to establish a relationship between microbands and deformation twins. Microbands are a unique feature of the crater-related microstructure in copper targets and may be unique to the cratering process in general, considering target materials which would have a normal propensity to twin, especially in plane-wave shock loading [25].

Finally, a simple phenomenological model for cratering in copper targets was developed which could be more generally applied to other metal targets by appropriately adjusting the microstructure development and residual microstructure zones.

Acknowledgements

This research was supported by a NASA–Johnson Space Center Grant NAG-9-481. We are grateful to Dr Fred Hörz (NASA-JSC) who provided the impact craters examined in this investigation.

References

1. S. A. QUIÑONES, J. M. RIVAS and L. E. MURR, *J. Mater. Sci. Lett.* **14** (1995) 685.
2. S. A. QUIÑONES, J. M. RIVAS, E. P. GARCIA and L. E. MURR, *J. Mater. Sci.* (1996) in press.
3. S. A. QUIÑONES, J. M. RIVAS, E. P. GARCIA, L. E. MURR, F. HÖRZ and R. P. BERNHARD, "Metallurgical and Materials Applications of Shock-Wave and High-Strain-Rate Phenomena", edited by L. E. Murr, K. P. Staudhammer and M. A. Meyers (Elsevier Science, New York, 1995) Ch. 39, p. 293.
4. A. C. CHARTERS and J. L. SUMMERS, US Naval Ordinance Laboratory Report NOLR-1238 (1959) p. 200.
5. B. G. COUR-PALAIS, *Int. J. Impact Eng.* **5** (1987) 221.
6. *Idem, ibid.* **5** (1987) 681.
7. R. KINSLOW (ed.), "High Velocity Impact Phenomena" (Academic Press, New York, 1990).
8. H. J. MELOSH, "Impact Cratering: A Geologic Process" (Oxford University Press, New York, 1989).
9. *Idem, Icarus* **59** (1984) 234.
10. *Idem, ibid.* **62** (1985) 339.
11. A. C. GUREVITCH, L. E. MURR, H. K. SHIH, C-S. NIOU, A. H. ADVANI, D. MANUEL and L. ZERNOW, *Mater. Charact.* **30** (1993) 210.
12. L. E. MURR, H. K. SHIH, C-S. NIOU and L. ZERNOW, *Scripta Metall. Mater.* **29** (1993) 567.
13. *Idem, Mater. Charact.* **33** (1994) 65.
14. F. JAMET and R. CHARON, "A flash X-ray diffraction system for shaped charge jets analysis", Report (0211/86) Franco-German Research Institute, Saint Louis, France, May 1986.
15. L. E. MURR, C-S. NIOU, J. C. SANCHEZ, H. K. SHIH, L. DUPLESSIS, S. PAPPU and L. ZERNOW, *J. Mater. Sci.* **30** (1995) 2747.
16. D. H. LASSILA, W. P. WALTERS, D. J. NIKKEL Jr and R. P. KERSHAW, in "Metallurgical and Materials Applications of Shock-Wave and High-Strain-Rate Phenomena", edited by L. E. Murr, K. P. Staudhammer and M. A. Meyers (Elsevier Science, New York, 1995) Ch. 60, p. 503.
17. A. H. CHOKSHI and M. A. MEYERS, *Scripta Metall. Mater.* **24** (1990) 605.
18. E. FERREYRA T., L. E. MURR and F. HÖRZ, in Metallurgical and Materials Applications of Shock-Wave and High-Strain-Rate Phenomena", edited by L. E. Murr, K. P. Staudhammer and M. A. Meyers (Elsevier Science, New York, 1995), Ch. 37, p. 303.
19. M. A. MEYERS, "Dynamic Behavior of Materials" (Wiley, New York, 1994).
20. L. E. MURR, "Electron and Ion Microscopy and Microanalysis", 2nd Edn (Marcel Dekker, New York, 1991).
21. J. M. RIVAS, S. A. QUIÑONES and L. E. MURR, *Scripta Metall. Mater.* **33** (1995) 101.
22. R. BULLOUGH and C. M. WAYMAN, *Trans. AIME* **236** (1966) 1704.
23. C. M. WAYMAN and R. BULLOUGH, *ibid.* **236** (1966) 1710.
24. J. C. SANCHEZ, K. P. STAUDHAMMER and L. E. MURR, in "Metallurgical and Materials Applications of Shock-Wave and High-Strain-Rate Phenomena", edited by L. E. Murr, K. P. Staudhammer and M. A. Meyers (Elsevier Science, New York, 1995) Ch. 96, p. 801.
25. L. E. MURR, in "Shock Wave and High-Strain Rate Phenomena in Metals", edited by M. A. Meyers and L. E. Murr (Plenum, New York, 1981) Ch. 37, p. 607.
26. M. A. MEYERS, U. R. ANDRADE and A. H. CHOKSHI, *Metall. Mater. Trans. (A)* **26** (1995) 2881.
27. P. J. JACKSON, *Mater. Sci. Eng.* **57** (1983) 39.
28. J. C. HUANG and G. T. GRAY III, *Acta Metall. Mater.* **37** (1989) 3335.
29. M. HALLOUIN, F. COTTET, J. P. ROMAIN, L. MARTY and M. GERLAND, in "Impact Loading and Dynamic Behavior of Materials", Vol. 2, edited by C. Y. Chiem, H-D. Kunze and L. W. Meyer (Informations gesellshaft, Bremen, Germany, 1988) p. 1051.
30. R. P. BERNHARD and F. HÖRZ, *Int. J. Impact Eng.* **17** (1995) 69.
31. F. HÖRZ, M. J. CINTALA, R. P. BERNHARD, F. CARDENAS, W. E. DAVIDSON, G. HAYNES, T. H. SEE and J. L. WINKLER, "Penetration Experiments in Aluminum 1100 Targets Using Soda–Lime Glass Projectiles", NASA Technical Memorandum 104813, NASA-Johnson Space Center, June 1995.
32. L. E. MURR, E. P. GARCIA, E. FERREYRA T., R. P. BERNHARD and F. HÖRZ, to be published.

Received 6 February
and accepted 18 March 1996